Geometric forward modeling of thrust systems underlying shortening landforms on Mercury

Stephan R. Loveless[1*], Christian Klimczak[1], Kelsey T. Crane[2], and Paul K. Byrne[3]

[1]Center for Planetary Tectonics, Department of Geology, University of Georgia, Athens, GA 30602, USA

[2]Seres Engineering & Services, LLC, Charleston, SC, 29492, USA. ktcrane@seres-es.com

[3]Department of Earth, Environmental, and Planetary Sciences, Washington University in St. Louis, Stl Louis MO, 63130, USA

*Corresponding Author, email: Stephan.Loveless@uga.edu

Abstract

Mercury hosts thousands of shortening landforms that are widespread across the entire planet. The shortening is widely accepted to be caused by a combination of thrust faulting and folding, resulting from the global contraction of Mercury caused by long, sustained cooling. Most shortening landforms on Mercury's surface have been classified into one of two groups: lobate scarps or wrinkle ridges. There is no distinct statistical difference in the surface morphology of these shortening landform classifications. Only a small subset of shortening landforms are clear-endmember wrinkle ridges and lobate scarps. The difference between geomorphic manifestations of shortening landforms may be governed entirely by the thrust systems and associated folding that form them. We therefore model thrust systems associated with 55 lobate scarp and wrinkle ridge endmember shortening landforms found across the surface of Mercury. Structures were modeled in 2D sections below the topographic profiles of landforms with the greatest structural reliefs. Models utilized the fault-bend fold algorithm in the MOVE geologic modeling software. Once models matched the observed topography and shortening strain, fault geometric parameters, such as number of structures, dip, depth extent of faulting, height, etc., were extracted and compiled for all structures. Our modeling shows that Mercury hosts a wide range of complex thrust systems, including single, listric faults, imbricate thrusts, and pop-up structures. In particular, the morphologies of lobate scarps end-member structures are best explained by models of a single, listric fault, whereas most wrinkle ridge end-member structures require more than one fault. We identify a large overlap in the variation of fault geometric parameters for both wrinkle ridge and lobate scarp archetypes, confirming the results of our previous geomorphic analysis that shortening landforms do not comprise two distinct categories. The overlap in geometric parameters also suggests that global contraction generated most of these structures.

1) Introduction

Mercury hosts a global population of positive-relief, tectonic shortening landforms as revealed by both the Mariner 10 (e.g., Strom et al., 1975) and MEcury Surface, Space ENvironment, GEochemistry, and Ranging (MESSENGER) missions (e.g., Byrne et al., 2018). Such landforms are thought to be produced by global contraction (e.g., Solomon, 1978) and are widely accepted to be formed by thrust faulting and folding (e.g., Strom et al., 1975; Byrne et al., 2014; Byrne et al., 2018). Many terms have previously been used to describe tectonic landforms formed by thrust faults, e.g., "shortening structures" or "thrust fault-related landforms", but for simplicity we will refer to all such structures as "shortening landforms" throughout this study.

Shortening landforms are common on all major rocky bodies in the Solar System. Such structures depict positive-relief cliffs, often paralleled by breaks along the surface (e.g., Schultz and Watters, 2001; Watters, 2003). Since the earliest observations of tectonic features on terrestrial bodies, shortening landforms have been categorized into groups based on surface morphology alone (e.g., Dzurisin, 1978; Strom, 1979). Of the different classifications used to describe shortening landforms, lobate scarps and wrinkle ridges have been used as designations for almost all shortening landforms found on Mercury's surface (e.g., Melosh and McKinnon, 1988; Watters et al., 2004). Lobate scarps are described to show clear linear-to-arcuate surface breaks in plan view, with topographic characteristics of steeply sloping forelimbs at the surface break trailed by gradual sloping backlimbs (Figure 1a; e.g., Strom et al., 1975; Strom, 1979; Watters, 1993). Such surface expression is linked to asymmetric anticlinal folding of the hanging wall (Byrne et al., 2014) with the asymmetry, or vergence, providing clear indication of tectonic transport to be in the direction in which the forelimb slopes (i.e., the vergence). This geometry is akin to the folding geometry of fault-displacement gradient folds described by Wickham (1995).

Wrinkle ridges have been described as having complex, sometimes sinuous map patterns in plan view that are accompanied by cross-sectional topographic profiles demonstrating a superimposed ridge (the "wrinkle") on top of a primary ridge (e.g., Watters, 1988). Shortening landforms of this class are common within volcanic plains of terrestrial planetary bodies throughout the Solar System (e.g., Plescia and Golombek, 1986; Nahm et al., 2023). On Mercury, wrinkle ridges frequently host faults that break at the surface (Strom et al., 1975; Watters, 1988; Golombek et al., 2001; Schleicher et al., 2019), but many have also been interpreted to be anticlinal folds above blind thrust faults (e.g., Schultz, 2000) containing backthrusts (Okubo and Schultz, 2004). Byrne et al. (2018) argued that wrinkle ridges host two oppositely facing monoclines which may indicate vergence of two opposing thrusts.

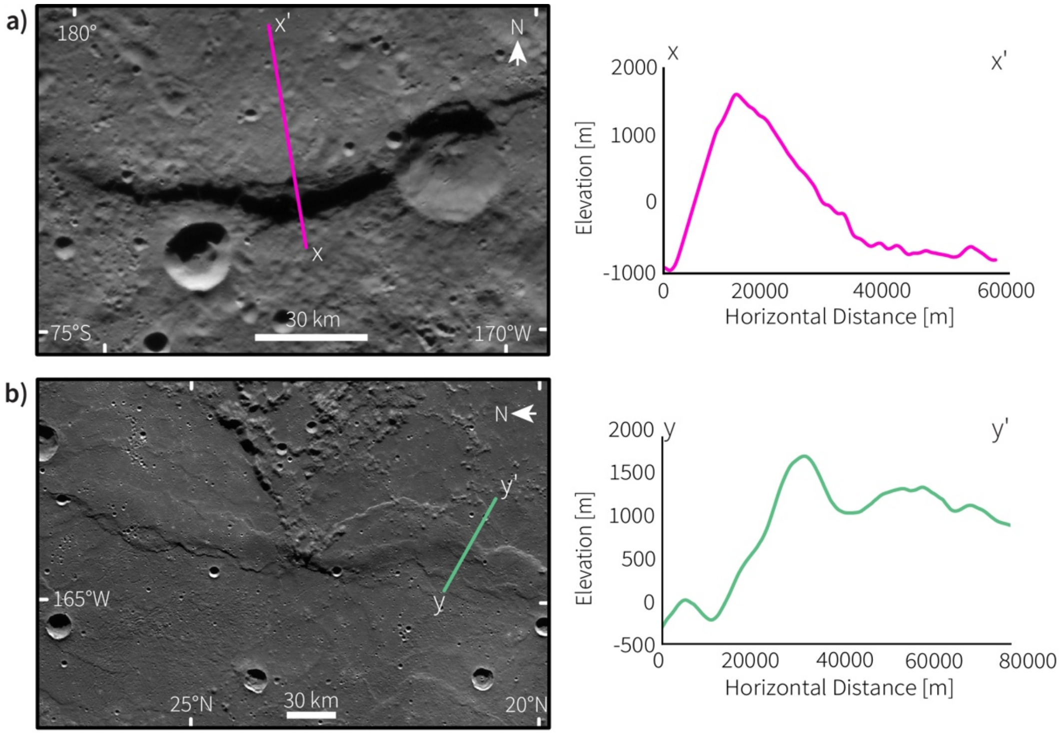

Figure 1: Examples of what have been classified as "lobate scarps" (a) and "wrinkle ridges" (b) on Mercury (modified after Loveless et al., 2024a). a) Map view of an unnamed lobate scarp near the south pole (left) with the corresponding topographic profile from x to x′ (right). b) Map view of Schiaparelli Dorsum, a prominent wrinkle ridge (left) with the corresponding topographic profile from y′ (right). Maps use a stereographic projection centered on the shortening landform. Both profiles are shown at ~16× vertical exaggeration.

The oversimplification that categorizing shortening landforms into these two groups is challenged by the large variation of thrust systems found on Earth. Mountain ranges that formed by shortening display a wide range of complex systems of thrust faults and folds (e.g., Chapple, 1978; Matthews and Work, 1978; McClay, 1978; McClay and Price, 1981; Boyer and Elliot, 1982; Morley, 1988; Crane and Klimczak 2019a). There is no evidence that suggests that thrust systems on Earth operate differently and therefore thrust systems on other planets should not be treated otherwise than those observed on Earth. Fold and thrust belts are common large-scale crustal shortening systems that are accommodated by multi-fault thrust complexes (e.g., McClay and Price, 1981). Common Earth thrust systems like duplex structures are described with listric or curved fault geometries with either stacked panels bounded by thrust faults or as imbricate thrusts with multitude of thrusts branching off a single décollement (Boyer and Elliot, 1982). Many of these thrust systems are created by displacement along multiple faults to build positive relief. In contrast, thrust systems on other planets are commonly interpreted as single, homoclinal (non-curved) fault planes (e.g., Schultz and Watters, 2001).

Few studies have suggested fault geometries on Mercury like to those on Earth. Some examples include for an extensive décollement underlying Beagle Rupes (Rothery and Massironi, 2010) and pop-up thrust system structure for shortening landforms and complex compound landforms on Borealis Planitia (Crane and Klimczak, 2019b). Other analogies between Earth and Mercury tectonics have been drawn from the conceptualization of thin- and thick-skinned deformation (Crane and Klimczak, 2019b). Thin-skinned deformation is strain accommodated by faults in weak upper horizons of the lithosphere (originally, for Earth, the sedimentary cover atop crystalline basement rock), whereas thick-skinned deformation is strain accommodated by faults that have penetrated deep into the basement (Chapple, 1978; Pfiffner, 2017). Analogies of thrust fault-related landforms to shortening structures on Earth have been made for thin-skinned tectonics features like the Yakima fold and thrust belt in Washington State (e.g., Watters et al., 2004), and the Lesser Himilayan Duplex (Crane and Klimczak, 2019b). Thick-skinned deformation has been used to describe Mercury's shortening landforms with comparisons to the Wind River thrust fault (Watters and Robinson, 1999; Mueller et al., 2014). Although impact-weakened stratigraphic horizons or volcanic layering are frequently invoked as layers permitting thin-skinned tectonics in volcanic plains, basement-reactivated thin-skinned tectonics has been invoked as a hybrid mechanism on Borealis Planitia (Crane and Klimczak, 2019b). By this mechanism, faulting and folding within the smooth plains are influenced by fault activity in the basement rock (Pfiffner, 2017).

Many previous subsurface modeling efforts for shortening landforms on rocky bodies have used the elastic halfspace mechanical dislocation COULOMB code (e.g., Schultz and Watters, 2001; Egea-González et al., 2012; Williams et al., 2013; Byrne et al., 2016; Egea-González et al., 2017; Peterson et al., 2020) or geometric cross-balancing techniques including trishear modeling (e.g., Herrero-Gil et al., 2019, 2020) or fault-propagation folding (Mueller et al., 2014). Using COULOMB, a set of physical parameters for a predefined fault plane are invoked as the surrounding lithosphere is elastically deformed to match the observed topography (Toda et al., 2005). Early studies modeled simple homoclinal faults with uniform displacements (e.g., Schultz and Watters, 2001) that can produce artifacts in the predicted topography if the superposed displacement is not tapered toward the fault tips. However, listric fault geometries have also been applied to COULOMB modeling to produce acceptable model topographies (e.g., Watters and Schultz, 2002; Byrne et al., 2016; Peterson et al. 2020), but other studies have found listric faults to inaccurately represent the uplifted topography (e.g., Egea-Gonźalez et al., 2012; Herrero-Gil et al., 2019). Alternatively, the trishear forward modeling technique recreates fault propagation folding, which uses cross-balancing techniques that relates folding deformation at the upper fault tip to a specialized limb angle and hinge ratios. These cross-balancing methods have been used in conjunction with faulted offset craters to model the underlying fault geometry (e.g., Mueller et al., 2014; Herrero-Gil et al., 2020). These methods come with a set of drawbacks. First, not every surface-breaking thrust fault has a superposed offset crater. Second, the trishear approach requires introducing additional geometric complexities and a wide, largely unknown parameter space associated with planetary shortening landforms.

The goal of this study is to investigate the variety of thrust systems in Mercury's subsurface. This is done by modeling 55 morphologically variable shortening landforms by selecting the endmember lobate scarp and wrinkle ridge structures from the data set published in Loveless et al. (2024b). To be concise, we refer to these endmember structures as lobate scarp archetypes and wrinkle ridge archetypes, however, we note that some wrinkle ridge endmember structures were classified as lobate scarps in the LDA of Loveless et al. (2024a). Our modeling utilizes the fault-bend fold algorithm in the MOVE geologic modeling software from PE Limited (Petex). Fault-bend folding is a proven geometric forward-modeling technique that can be applied to fault displacement-gradient folds (e.g., Suppe, 1983; Medwedeff and Suppe, 1997; Brandes and Tanner, 2014; Hughes et al., 2014; Connors et al., 2021). We collect and synthesize fault geometric parameters for our 55 models to identify the structural characteristics of shortening landforms on Mercury.

2) Methods

2.1) Landform selection

We previously assessed the morphological variability of 100 randomly selected shortening landforms on Mercury to distinguish lobate scarps and wrinkle ridges (Loveless et al., 2024a; Figure 2). In particular, we conducted a Linear Discriminant Analysis (LDA) that maximizes the difference between two predefined groups by creating a linear equation that classifies cases based on their correlated parameters. An LDA used to distinguish two groups assigns to each case a positive or negative value, or linear discriminant (LD) for its classification. For example, an LDA of lobate scarps and wrinkle ridges shows a large degree of overlap in the LD (Fig. 2; Loveless et al., 2024a), indicating that the morphology of these shortening landforms on Mercury does not support distinct groups. To further investigate if a structural difference between these categories exists, we use the end members of the lobate scarps (n=30) and all of the wrinkle ridges (n=25; Figure 2) to model their underlying thrust systems. We use the terms lobate scarp archetypes and wrinkle ridge archetypes when referencing these lobate scarp and wrinkle ridge shortening landforms that we model in this work.

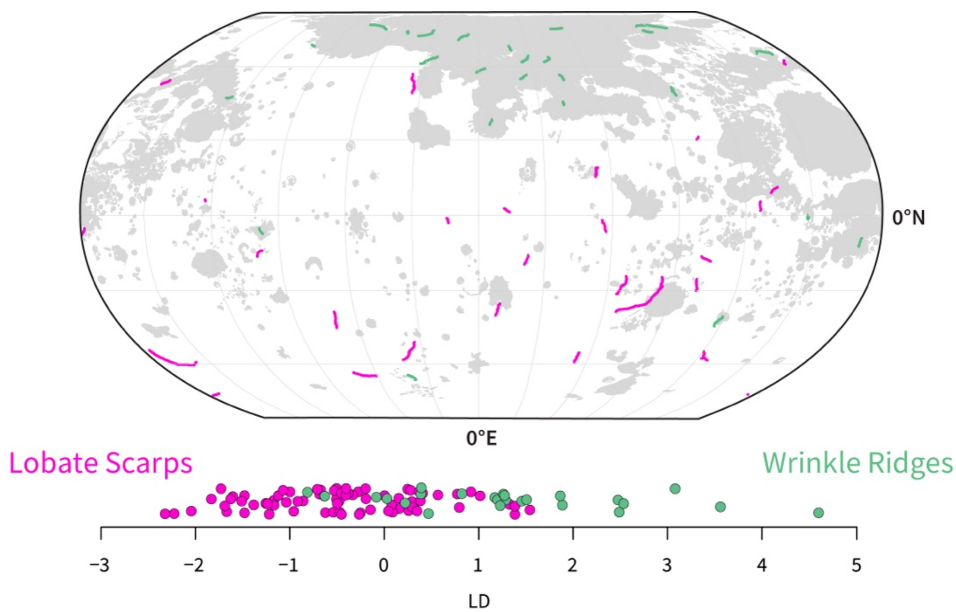

Figure 2: Global distribution of 55 shortening landforms modeled in this study shown in Robinson projection. Landforms traditionally identified as lobate scarps are shown in magenta, while those previously identified as wrinkle ridges are shown in green. For reference, the smooth-plains units (Denevi et al., 2013) are shaded in gray. The LDA analysis of the 100 shortening landforms assessed in Loveless et al. (2024a) is shown on the LD axis below.

2.2) Modeling

We construct models using the 2D Move-On-Fault module in the MOVE modeling software by PE Limited (Petex). Our models make use of the Fault-Bend Fold algorithm, which is a geologic restoration technique that directly relates folding in the hanging wall of the fault to the shape and displacement along the fault plane. Describing deformation as a fault-bend fold uses structural balancing, which is the integration of satisfying a set of conditions between the interpreted initial state and observed deformed state of the area or volume of interest (Dalhstrom, 1969). Such conditions include the maintenance of length of the interpreted geologic horizons pre- and post-deformation.

A fault-bend fold is a fault-related geometry, where folding of the hanging wall is caused by distortions along the fault plane (Suppe, 1983). The relationship between the slip along the fault plane and the folding of the above horizons is modeled through a series of trigonometric relationships dependent on changes of the fault dip. The specific shape of the fault and the amount of along-slip displacement govern the distorted shape of the overlying layers of rock. Whereas a homoclinal fault experiencing simple shear accommodates all of the shortening through the displacement along the fault, a fault-bend fold will drive different amounts of shortening accommodated along the fault plane through a combination of slip and folding arising from changes in the dip of the fault plane. Homoclinal portions of a fault in a fault-bend fold will accommodate shortening with more slip, and as the fault changes dip, or ruptures the surface, folding becomes more prevalent. The faults modeled in this study break the surface, so the fault-bend fold geometry simulates how the uplifted hanging wall folds over the footwall.

Such geometric configurations have been used for many years to characterize contractional tectonic architecture on Earth (e.g., Suppe and Namson, 1979; Suppe, 1983; Connors et al., 2021). Fault-bend folds are present in seismic reflection profiles of contractional tectonics on Earth (e.g., Shaw et al., 2005). Fault-bend fold architectures have also been used to describe or model the structural geology of shortening landforms on Mercury (Byrne et al., 2018, Crane and Klimczak, 2019b; Crane, 2020a). This type of fault geometry is a good representation of surface-breaking thrust faults for which displacements are large enough to permit the hanging wall to fold over the footwall.

We model the fault structure under each of our selected shortening landforms along the inferred direction of tectonic transport and at the point of highest structural relief along the topographic profile. The direction of tectonic transport is assumed to be perpendicular to the long axis of a landform, except where an impact crater is crosscut and shortened by the fault, indicating the direction of displacement (Galluzzi et al., 2015). The selected topographic profile is then imported into the MOVE software and 50 arbitrary, evenly spaced horizontal geologic horizons are constructed underneath the topographic profile to track the modeled deformation. The uppermost of these horizons is taken as the planetary surface. The elevation of this surface horizon is set equal to the measured elevation at the start of the forelimb. We vary the specific spacing of the horizons based on the length of the landform.

After the horizons are constructed, we draw a fault plane within the model setup. We conduct the modeling while simultaneously assessing the photogeology of the shortening landform to accurately inform the model with all of the available observations. Initially the fault is assumed to be a homoclinal fault plane with a reverse sense of slip and a dip angle of 30°. Iterative model previews are generated as the fault plane geometry, depth, and displacement are changed until the modeled surface horizon matches the observed topography. Fault parameters were adjusted based on the results from the previous models by raising or lowering areas the fault in the respective areas of the surface that needed alterations. The amount by which a fault was changed is relative to the discrepancy between the modeled surface and the observed surface in the previous model. Once the observed topography is matched, we calculate the shortening strain from folding for our model to test against the observed shortening strain as an additional control point. More details on this control point are provided in Section 2.3. A model is deemed to be a successful match once the modeled topography matches the observed topography within 10% of the maximum relief of the structure and the shortening strain from folding of the model matches within 0.2% of the observed shortening strain across the structure (Loveless et al., 2024b).

If two or more surface breaks are present on image data, then we include more than one fault in the model. In this case, we model the primary fault first, which we determine using photogeological observations. The geometries and displacements of any other faults are subsequently added to replicate the desired deformation.

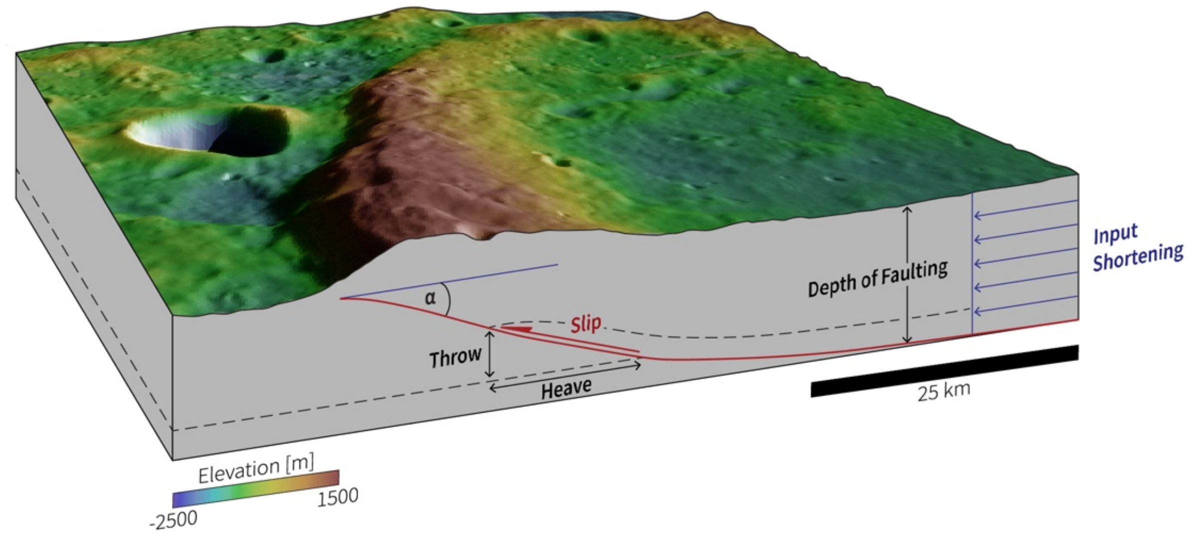

Figure 3: Block diagram of a shortening landform with stylized fault plane to highlight the fault geometric parameters extracted from each model. The dashed line in the subsurface represents an arbitrary marker horizon to depict deformation along the fault. The image in this figure is taken from the MESSENGER low-incident angle global mosaic (Denevi et al., 2017). Elevation data are from Bertone et al. (2023).

Once a model was complete, 13 modeled fault parameters were extracted (Figure 3), including near-surface fault dip, average dip, maximum dip, input shortening, average heave, average throw, average slip, maximum slip, depth of faulting, fault height, and modeled strain from folding. *Near-Surface Fault Dip* is defined as the dip of the fault in the uppermost 10% of the fault. *Average Dip* (α in Figure 3) is the average downward angle the fault makes with a horizontal plane, and *Maximum Dip* is the maximum downward angle relative to a horizontal plane. All dips are measured in degrees. *Input Shortening*, measured in kilometers, is the horizontal shortening implemented in the Fault-Bend Fold algorithm to which the model displaces the deformed horizons.

The slip accommodated along a fault in a fault-bend fold structure varies along the height of the fault (Suppe, 1983); therefore, we include additional measurements from our models. *Average Heave* and *Average Throw*, both measured in kilometers, are the average horizontal and vertical components of the displacement laterally along the fault. *Average Slip* is the average displacement laterally along the fault. *Maximum Slip* is the maximum amount of displacement that occurs along the fault. Other measurements include *Depth of Faulting*, measured in kilometers, as the depth extent measured vertically from the surface to the lowermost portion of the fault and

Fault Height, measured in kilometers, which is the down-dip length of the modeled fault plane (red line in Fig. 3). From fault height, we calculate *Aspect Ratio*, which is the fault height divided by the mapped length of the fault taken from Loveless et al. (2024b). If more than one fault was needed for a model, the fault height of the largest of the faults is reported. *Number of Faults* is the number that was needed to model the observed deformation for each landform. Finally, the modeled strain from folding of the uppermost hanging-wall horizon produced by the model is calculated as:

$$\varepsilon_{\mathrm{Fold}} = \frac{\mathrm{L_H} - \mathrm{L_T}}{\mathrm{L_T}},$$

where $\mathrm{L_H}$ is the horizontal hanging wall horizon length and $\mathrm{L_T}$ is the total hanging wall horizon length.

Thrust System Type and *Fault Shape* are two qualitative metrics that describe the subsurface structure of the shortening landforms. *Thrust System Type* refers to the number of faults (one, two, or three) and their respective directions of tectonic movement, or direction of tectonic transport from one another. *Fault Shape* describes whether the fault plane is listric (curved) or planar.

2.3) Controls of the models

As for cross-section restoration and balancing, a model can be deemed successful once it satisfies all control parameters. For geologic restoration of studies on Earth, such controlling parameters include interpretations of seismic sections and lithologic changes and repeated or missing sequences in borehole data (e.g., Egan et al., 1997; Pierdominici et al., 2011). Fault geometry, depth, and dip can be directly correlated to the seismic response of faults in the subsurface, and surface dips from *in situ* field measurements can all serve as controls.

For other terrestrial planets, subsurface data and *in situ* analyses are more difficult or impossible to obtain. The current standard of fault modeling efforts in the past has been to match the topography by forward modeling of an initially undeformed surface. This technique has been applied to many bodies that host faulting such as Mercury (e.g., Watters et al., 2016; Crane, 2020b), the Moon (e.g., Williams et al., 2013; Byrne et al., 2015; Collins et al., 2023), and Mars (e.g., Schultz and Watters, 2001; Herrero-Gil et al., 2019). Topography is a reasonable control for these bodies because they lack substantial surface erosion. However, forward modeling can produce more than one solution for the same topography (Egea-González et al., 2017), and that there is an element of non-uniqueness to such modeling. Therefore, for our modeling efforts we use the matching the topography within ±10% of the structure's vertical relief as the minimum criterion to be met for a model to be deemed acceptable. This is done by creating copies of the topographic profile at elevations ±10% of the vertical relief and forward modeling the surface until it lies between those boundaries.

To maximize the likelihood of producing a unique solution for our models, we must use additional control points aside from the observed topography. To better constrain our models, the modeled strain from folding must be as close as possible to the observed shortening strain. The observed shortening strain values are taken from Loveless et al. (2024b). These values were calculated as the change in length (landform breadth minus the total cross-sectional length) divided by the total cross-section length. In a fault-bend fold, shortening along the fault is accommodated by both the heave (the horizontal component of displacement) and by folding of the hanging wall. The amount of strain accommodated by folding is a function of the shape of the fault.

At the surface, the amount of shortening accommodated by folding is governed by the depth of faulting, input shortening, and variations of the fault dip (See Section 3). A deeper modeled fault requires less input shortening to match the actual topography as more material displaced from depth to the surface, but more folding will be accommodated at the surface. An increase in modeled depth of faulting increases the strain from folding. Alternatively, more shallowly penetrating faults require greater shortening, but the modeled strain from folding will decrease. Therefore, a unique solution for fault depth, input shortening, and fault dip is achieved by matching the modeled strain from folding to the observed shortening strain values in addition to matching the modeled topography with the observed topography.

We try to match the modeled strain from folding to the observed shortening strain values exactly but find negligible changes in the overall fault geometry in a ±0.2% range of the modeled strain from folding. We summarize our strain-matching efforts with box-and-whisker plots, a non-parametric way to portray variance (Figure 4). The distribution of the sample size for our modeled strain from folding and the distribution of the observed shortening strain from the same landforms compiled from Loveless et al. (2024b) aligns well (Figure 4). We interpret this as an indication that our models provide a good representation of the folding at the surface and the subsurface fault architecture of the shortening landforms.

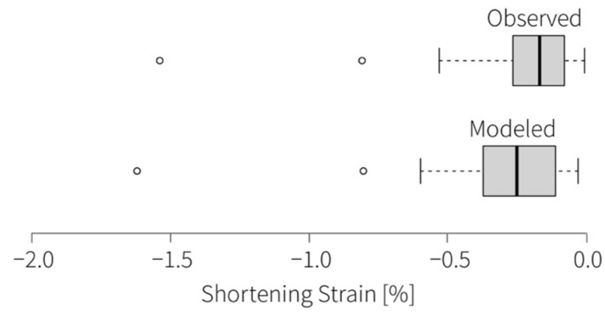

Figure 4: Box and whisker plot of the observed strain from folding compared with the modeled strain from folding. Bold lines indicate the median, the left and right edges of the gray box are the first and third quartiles, and maxima and minima are indicated by the vertical segments. Outliers are shown as dots.

On Mercury, some shortening landforms crosscut craters. If a crater is assumed to be initially circular, the overall shortening deformation of the cut crater can be used to constrain geometric properties of the fault, such as fault dip and displacement vector (Galluzzi et al., 2015), which can be another control point for a structural model. Most of the shortening landforms selected in our study do not crosscut craters, and if they do, the craters are either not adequately deformed enough to extract any meaningful structural information or are located far from our cross-section line and so do not contain the exact information needed for our model. Only in a couple instances does this method work in our sample of shortening landforms as this method works only on well-preserved craters. For 11 of the 55 landforms, deformed craters were present near the cross-section. However, most of the faults assessed in this work that show cross-cutting relationships with craters do not unequivocally show the direction of tectonic transport. Therefore, this is a valid control point that is considered but is only used for a small subset of our sample size.

3) Sensitivity study

We conducted a sensitivity study to test the efficacy of our workflow, the impact of control points, and the resulting fault geometries. For that, we construct three models for the same shortening landform (Figure 5). All models satisfy the topographic control point and match the direction of tectonic transport from a nearby shortened crater but vary with fault geometric parameters (Table 1). Out of the three, only one satisfies the second control point by matching the modeled to the observed strain from folding. In Model 1, we construct a fault that matches the observed topography and that penetrates to 11.4 km and dips an average of 9°, leading to a slip on the fault of ~5700 m from an input shortening of 5500 m. In Model 2, we construct a fault that matches the same topography but penetrates to a depth of 24.2 km and dips at an average 21°.

Model 2 requires an input shortening of 2400 m producing a slip along the fault of 2800 m. The fault for Model 3 also was constructed to match the input topography, but penetrates to 48.1 km, dips at an average of 40°, and requires 850 m of shortening to produce 1673 m of slip on the fault.

The shortening strain observed along the landform for all three models is –0.806%. The modeled strain from folding is –0.622%, –0.801%, and –1.255% for Models 1 to 3, respectively (Table 1). The modeled strain from folding of Model 1 matches the observed folding strain with a percent match of 77.2%. The modeled strain from folding of Model 2 most closely resembled the observed folding strain matching at 99.4% of the observed value. Model 3 has a percent match of 31.9% to the observed folding strain. Model 2 represents a successful model that both matches the observed topography and accords with the observed folding strain. The result of this sensitivity study highlights the dependence of the modeled strain from folding on the depth of faulting, dip of the fault, and input shortening. Therefore, by using both topography and the strain produced from folding as control points, we produce well constrained solutions of our shortening landform models.

Table 1: Comparison of parameters for the three subsurface models of the same shortening landform in Figure (4) Input shortening is a constraint of the model.

Parameters	**Model 1**	**Model 2**	**Model 3**
Observed Folding Strain [%]	-0.81	-0.81	-0.81
Modeled Strain from Folding [%]	-0.62	-0.80	-1.36
% of Match Modeled to Observed Folding Strain	77.2	99.4	31.9
Input shortening [km]	5.5	2.4	0.9
Depth of Faulting [km]	11.4	24.2	48.1
Average dip [°]	9	21	40
Maximum slip [km]	5.9	3.2	2.3

In a fault-bend fold, the strain accommodated by folding varies fault geometry (Figure 5, Table 1). Therefore, matching the observed and modeled folding strain plus the observed topography yields unique, doubly constrained solutions for the underlying fault geometry. Folding at the surface is directly related to the dip and depth of faulting. For the same landform, a fault penetrating to greater depths will have a greater dip than those penetrating to shallower depths. Slip in fault-bend folds decreases with steeper dips while greater amounts of deformation are accommodated by antiformal folding (Suppe, 1983). Therefore, our models produce less folding if the modeled fault penetrates to shallower depths, and the average slip along the fault increases (Table 1).

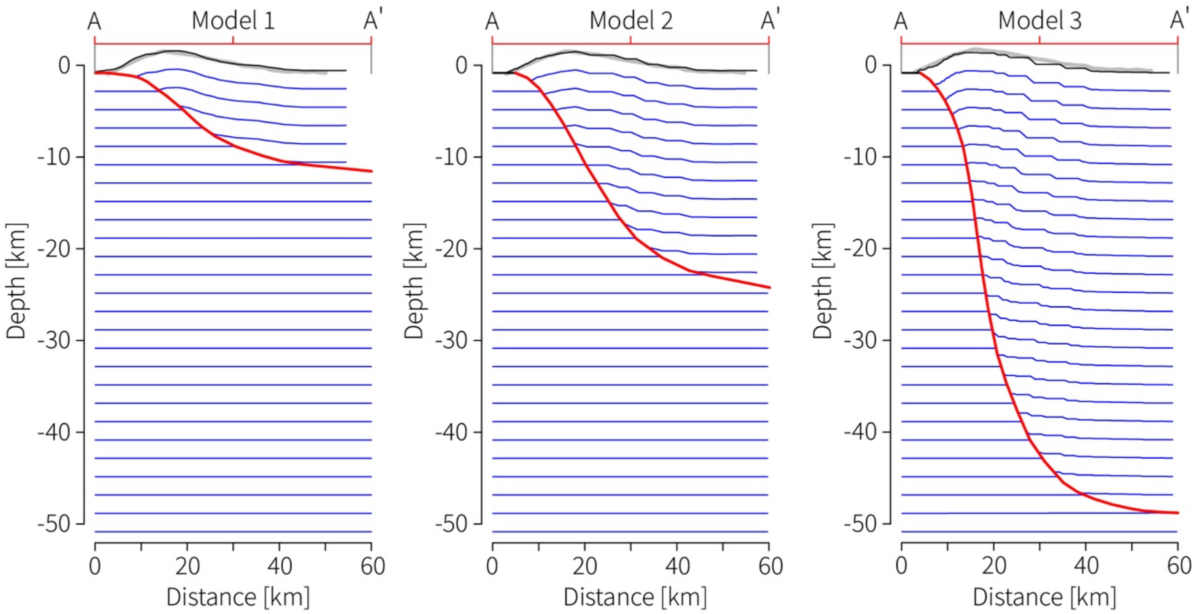

Figure 5: Three thrust fault models replicating the topography of the shortening landform depicted in Figure (3). All models are shown with 2× vertical exaggeration. Red line is the modeled fault. Blue lines are arbitrary horizons used to visualize subsurface deformation. Gray lines are observed topography; black, the modeled topography.

Larger amounts of input shortening and thus slip along the fault are needed to uplift the hanging wall block to match the topography (Model 1, Figure 5). This increases the total shortening strain of the surface, with consequently less strain accommodated by only the folding (Model 1, Table 1). We interpret such fault geometry as overestimating the accommodated shortening but producing faults that are too shallow with too gentle dips. Faults penetrating deeper need lower amounts of input shortening and so accommodate more folding at the surface (Model 2, Figure 5). Model 2 is the best-fit solution in which the model matches the observed topography and strain from folding, and so we take the modeled fault geometry as the best representation of reality. The smallest amount of input shortening, largest fault dip and deepest extent of fault produce equally good topographic matches, but the modeled strain from folding exceeds the observed strain (Model 3, Table 1). This model likely underestimates the accommodated shortening while producing very deep faults that dip too steeply.

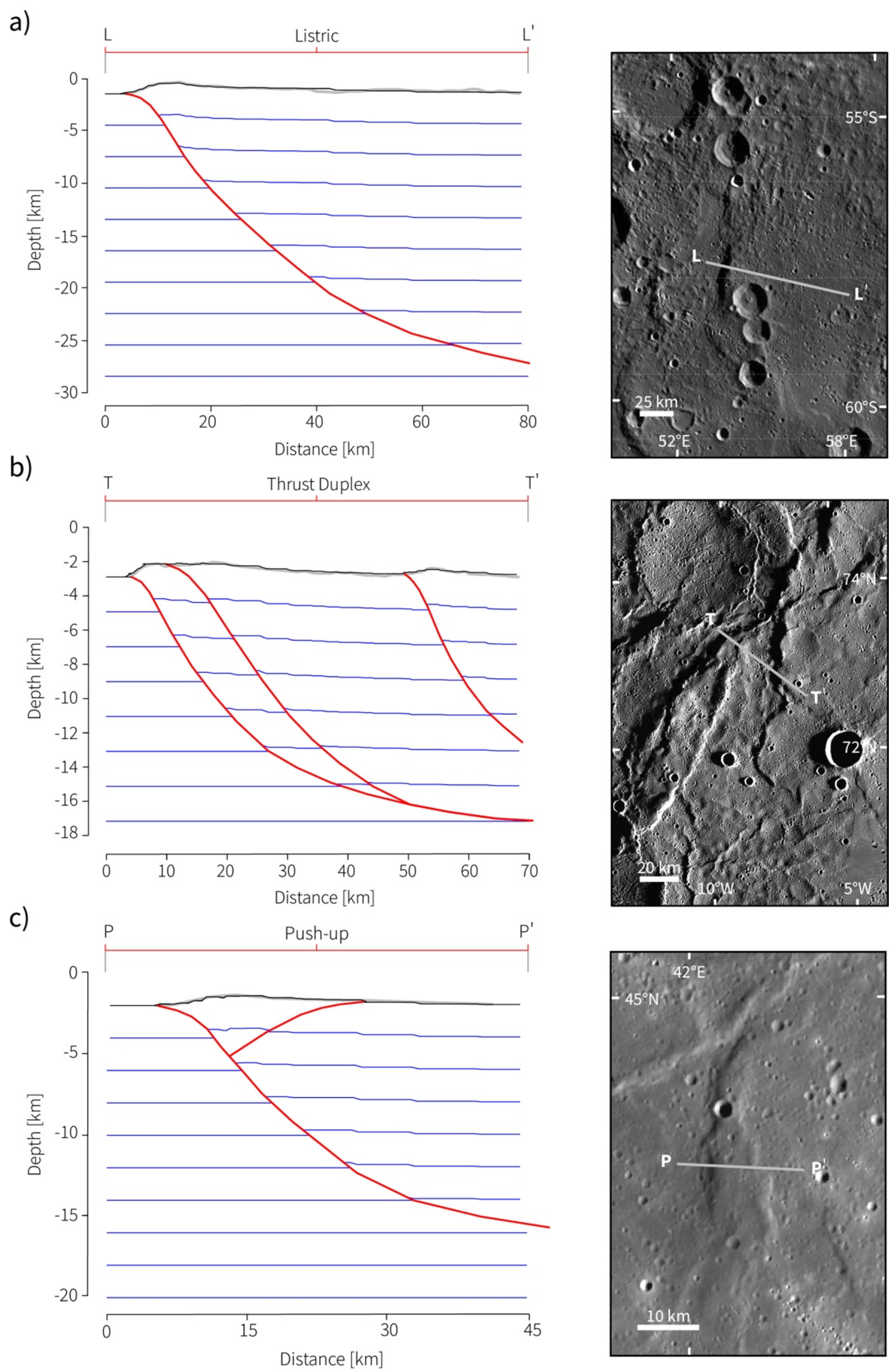

Figure 6: Three different thrust fault systems from Mercury with subsurface models shown on the left and map view on the right panel. a) An example of a single, listric fault (1.8× vertical exaggeration). b) An imbricate thrust (3.0× vertical exaggeration). c) A pop-up structure (1.8× vertical exaggeration). Model line colors are the same as in Figure (5).

4) Results

We applied our workflow and matched the two or, where possible, three controls to model the thrust systems of 55 shortening landforms on Mercury. From these models, 13 values were compiled to study the variability of these thrust systems. Additionally, thrust system type and overall fault shape (i.e., listric or homoclinal) was specified for each landform. We summarize our observation in a catalogue containing 30 lobate scarp and 25 wrinkle ridge archetypes. The summary of observations and individual MOVE models are published in the online repository accompanying this paper (Loveless et al., 2024c).

4.1) Thrust System Types

Among the 55 landforms, we modeled thrust systems that can be described as having one of three general geometries. The most prominent thrust system type we model are *single, listric faults* (Figure 6a), with 38 shortening landforms showing this geometry. In these thrust systems, the depth and curvature of the fault dictate how the hanging wall is folded. The large variety of modeled listric fault shapes span the entire range of modeled fault parameters, accommodating small and large strains and lithospheric penetration depths from <10 km to as deep as ~50 km.

The remaining 17 modeled thrust systems have multiple faults. Of those, we modeled seven *imbricate thrusts* (Figure 6b). These are a series of sub-parallel thrusts for which tectonic transport is occurring in the same direction and that may be rooted by a floor-thrust or décollement (Boyer and Elliot, 1982). Such structures are known on Earth to consist of overlapping, stacked series of blocks of rock separated by subparallel thrust-faults (Hopgood, 1987). Imbricate thrusts were modeled to occur underneath shortening landforms that displayed vergence in the same or nearly the same direction and to be tectonically related by their geographic proximity to one another or by their map patterns. In some instances, the vergence may change along the length of the shortening landform resulting in possible changing thrust system geometries underneath the shortening landform. This phenomenon occurs at the shortening landform shown on the right panel of Figure 6b. Along the surface break towards the southwest, one of the shortening landforms changes vergence and thus may transition from an imbricate thrust to a pop-up structure.

Indeed, *pop-up structures* comprise the third thrust system type we identified, of which we modeled 10 of them. Pop-up structures were interpreted to occur under those shortening landforms that have two or more sets of tectonic vergence in opposite directions (Figure 6c). These pop-up structures host a central crustal block that has been uplifted due to two oppositely dipping thrust faults that border its sides, where the bigger structure is the primary thrust and the smaller structure the secondary or back thrust (Butler, 1987). Generally, pop-up structures on terrestrial planets are found to vary in terms of the size relation of the primary thrust and secondary thrust. Most pop-up structures we model on Mercury, however, show a primary thrust that greatly exceeded the size of the back thrust in terms of fault depth and height, similar to the example in Figure 6c.

4.2) Comparison Between Shortening Landform Archetypes

We average all of the parameters generated by the modeled shortening landforms in this work (Table 2). Across all structures, the average near surface fault dip, average dip, and maximum dip are 21°, 22°, and 40°, respectively. The average input shortening for all shortening landforms is ~1.5 km. The mean values for average heave, average slip, maximum slip, and average throw are 1.2 km, 1.4 km, 1.6 km, and 0.6 km, respectively. The average depth of faulting across all shortening landforms is 21.9 km and the average fault height is 65.4 km. The sample of shortening landforms in this work produced a modeled strain from folding of –0.28%.

We compiled the parameters of our models to analyze their averages and variability for the wrinkle ridge ($n = 25$) and lobate scarp archetypes ($n = 30$) for their comparison. First, we averaged each parameter for each archetype landform to identify what defines a typical lobate scarp and wrinkle ridge on Mercury; the results are presented in Table (2). The representative thrust fault architecture underlying a lobate scarp archetype is a single, listric thrust fault that shallows with depth (e.g., Figure 5 Model 2; Figure 6a). These shortening landforms have an average dip of ~26° and fault to depths of ~27 km. The faults accommodate an average of ~2 km of slip and produce an average of –0.4% of modeled shortening strain from folding in the hanging wall.

The typical trust system underlying a wrinkle ridge archetype requires more than one fault, either as imbricate thrusts (Figure 6b) or pop-structures (Figure 6c). The most representative wrinkle ridge archetype model is shown in Figure 6c. Such shortening landforms are underlain by faults with an average dip of ~19° that penetrate to depths of ~13 km. These structures accommodate an average slip of ~0.7 km and produce an average of –0.16% of modeled shortening strain from folding in the hanging wall.

Second, we compute box-and-whisker plots for the aspect ratio, depth of faulting, the maximum and average dip angles, the maximum and average slip, the input shortening, and the shortening strain from folding (Figure 7) to document and compare the variability of the fault geometries associated with wrinkle ridge and lobate scarp archetypes on Mercury. We find that these parameters capture all aspects of modeled fault geometries. As with Figure (4), the bold lines within the boxes indicate the median value for each distribution, whereas the upper and lower bounds of the boxes are the first and third quartile values of each distribution. Minima and maxima data are indicated by the bounds of the line segment. Statistical outliers are shown as hollow dots along the axis.

Table 2: Averaged values of modeled parameters for lobate scarp and wrinkle ridge archetypes. Medians and ranges of these modeled parameters are shown in Figure 7.

Modeled Parameter	All Shortening Landforms	Lobate Scarp Archetypes	Wrinkle Ridge Archetypes
Near Surface Fault Dip (°)	21	25	17
Average Dip (°)	22	26	19
Maximum Dip (°)	40	43	36
Input shortening (km)	1.5	2.0	1.0
Average Heave (km)	1.2	1.7	0.7
Average Slip (km)	1.4	2.0	0.7
Maximum Slip (km)	1.6	2.2	0.9
Average Throw (km)	0.6	0.8	0.3
Depth of Faulting (km)	21.9	27.4	13.3
Fault Height (km)	65.4	90.0	64.5
Modeled Strain from Folding (%)	–0.28%	–0.39%	–0.16
Number of Faults	1.36	1.12	1.7
Aspect Ratio	0.41	0.44	0.28

The majority of aspect ratios for both wrinkle ridge and lobate scarp archetypes fall between 0.1 and 0.6 (Figure 7a). The average aspect ratio among all shortening landforms is 0.4. The range of aspect ratios for lobate scarp archetypes is from 0.1 to 1.3. Wrinkle ridge archetypes have an aspect ratio range of 0.1 to 1.4. Both archetypes show large overlap, but generally lobate scarp archetypes have higher aspect ratios as a result of their greater relief with respect to their lengths than wrinkle ridge archetypes do. We also find that lobate scarp archetypes penetrate to greater depths than their wrinkle ridge archetype counterparts (Figure 7b). Lobate scarp archetypes host faults that penetrate to depths of 8.4 km to 48 km, whereas the range of wrinkle ridge archetypes depth of faulting spans from 1.9 km to 38 km. These ranges of depths are nearly identical as only 6 lobate scarp archetypes are modeled to fault at depths greater than 38 km and only 7 wrinkle ridge archetypes are modeled to fault at depths less than 8.4 km.

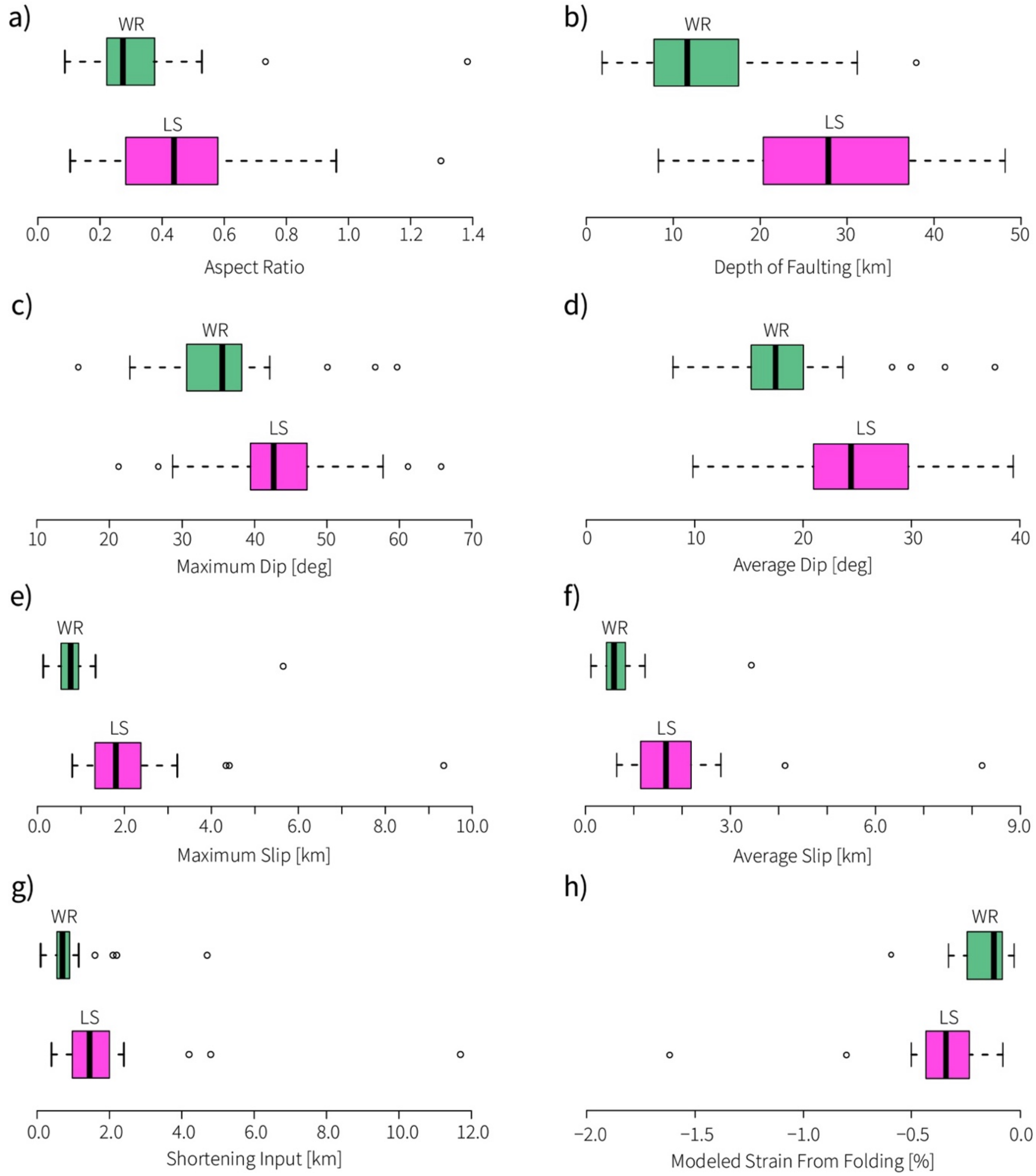

Figure 7: Box-and-whisker plots for eight parameters of our model solutions, showing the distributions of fault geometries of wrinkle ridge and lobate scarp archetypes on Mercury. These plots show comparisons of: (a) aspect ratios; (b) depth of faulting; (c) maximum dip; (d) average dip; (e) maximum slip; (f) average slip; (g) input shortening; (h) modeled strain from folding.

Lobate scarp archetypes host faults with a median maximum and a median average dip of 43° and 24° respectively (Figure 7c and d). Wrinkle ridge archetypes dip more shallowly than lobate scarp archetypes with a median maximum dip of 36° and a median average dip of 17°. The range for both maximum and average dip values overlap for both wrinkle ridge and lobate scarp archetypes. The maximum dip angle for lobate scarp archetypes ranges from 21° to 66° and wrinkle ridge archetype maximum dip angles ranges from 16° to 60° (Figure 7c), almost covering the same range of dip angles.

For both maximum and average slip values, wrinkle ridge archetypes overlap with the lower extent of lobate scarp archetype values (Figure 7g and h). A similar trend is shown in the ranges of input shortening values for wrinkle ridge and lobate scarp archetypes, where wrinkle ridge archetypes overlap with the lower extent of lobate scarp archetype values. The modeled strain from folding for wrinkle ridge and lobate scarp archetypes also demonstrates considerable overlap (Figure 7h). More negative values of modeled strain from folding indicate a greater amount of folding. Wrinkle ridge archetypes show less modeled shortening strain from folding than lobate scarp archetypes, but almost the entire range of wrinkle ridge archetype values falls within the lower range of modeled strain from folding values for lobate scarp archetypes.

4.3) The largest shortening landform on Mercury: Enterprise Rupes

Enterprise Rupes is widely regarded as one of the largest shortening landforms on Mercury's surface (e.g., Ferrari et al., 2015; Watters et al., 2016; Byrne et al., 2018) so we include it in our analysis (Figure 8a). Its highest vertical relief exceeds 3 km, and it has a mapped fault length of ~1000 km (Loveless et al., 2024b). Owing to its size, Enterprise Rupes was statistically classified with the highest lobate scarp designation in Loveless et al. (2024a). Enterprise Rupes is located in the southern hemisphere and crosscuts multiple impact craters including Rembrandt Basin: a large, 715 km diameter impact basin. Its highest structural relief towards the southeastern portion of its surface break. In this region, Enterprise Rupes is unaffected by large impacts or the geology of the Rembrandt basin, which is host to other smaller impacts, extensional and contractional tectonic features, thus providing an ideal cross-section to model the subsurface structure solely as it relates to the underlying fault architecture.

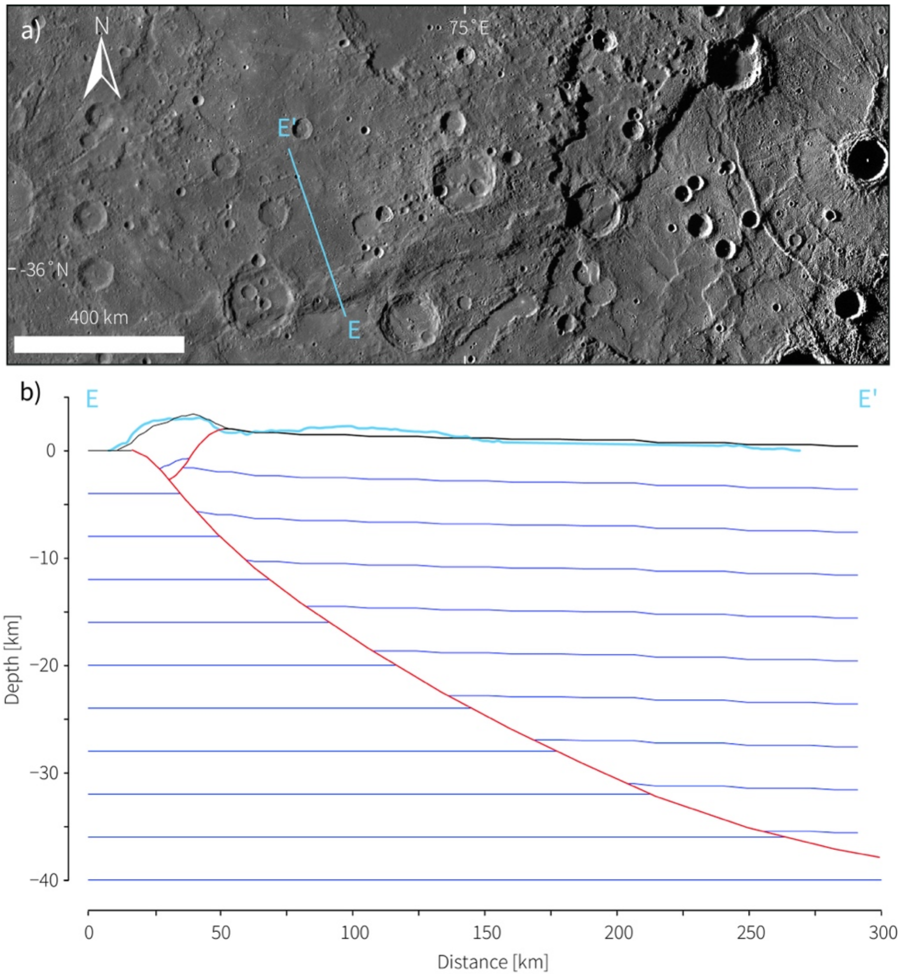

Figure 8: Top panel depicts the photogeology of Enterprise Rupes. Bottom panel depicts the model constructed underneath the transect E to E' in the image. Color coding is the same as in Figure (5) but observed topography corrected for anomalous topographic variations is shown in light blue. Model and topography in 4× VE.

Northwestward along the surface break, there are notable topographic highs that are likely unrelated to the deformation produced by the primary fault that formed Enterprise Rupes. To better constrain the shortening strain of Enterprise Rupes, we subtract these topographic variations from the observed topography (light blue line, Figure 8b). The displacement and strains generated by our model can therefore be assumed to be a lower bound for the possible displacements and strains. In this region, the morphology of Enterprise Rupes indicates two fault surface breaks and forelimbs with opposing vergence. The primary direction of tectonic transport along Enterprise Rupes is towards the southeast, as indicated by the pronounced forelimb along much of the structure and the multiple impact craters that Enterprise Rupes crosscuts.

The vertical relief at this area has been measured to be 3.3 km (Loveless et al., 2024b). The backlimb beyond the pop-up created by the oppositely verging thrust is also uplifted. To achieve such relief, a model input of 9 km of shortening was applied to the main thrust. The role of the secondary thrust only affects the peak at the tip of the shortening landform. The input shortening for this thrust was 2.7 km. These input shortenings for the primary and secondary thrusts translated to a maximum slip value of 9.3 km and 2.7 km, respectively. The primary fault has an average dip of 9° and a maximum dip of 17°. The secondary fault has an average dip of 11° and a maximum dip of 21°. The lower average dip angles are because of the extensive listric architecture of the fault geometry. We model Enterprise Rupes to fault to a depth of 34 km. The modeled strain from folding for Enterprise Rupes is –0.13, which is less than the median value of –0.34 found among lobate scarp archetypes (Figure 7h). However, the maximum slip, average slip, and slip components (average heave and throw) for Enterprise Rupes are, unsurprisingly, the largest values modeled in our data set.

5) Discussion

5.1) Lobate Scarp and Wrinkle Ridge Archetype Thrust Systems

We modeled the subsurface structure of 55 shortening landforms on Mercury to learn about the thrust systems that generated them. The results of our study show a large variation of fault geometric parameters (Figure 7). This finding demonstrates that thrust systems on Mercury are complex and host a large variation of thrust geometries, similar to what is observed in thrust systems on Earth. Based on a linear discriminant analysis of the shapes of these landforms (Loveless et al., 2024a), we selected those shortening landforms for our modeling that showed the biggest differences to one another with the intention of analyzing the broadest variation of thrust system morphologies that occur on Mercury's surface. We interpret the large variation of dip angles, depth of faulting, and slip as indicative of highlighting the innate complexities of Mercury's thrust systems.

The morphology of shortening landforms on Mercury supports wrinkle ridges and lobate scarps as endmember categories on a spectrum of shortening landforms (Loveless et al., 2024a). The results in this study provide additional support for these as archetypes as the average values for all shortening landforms consistently lie between average parameter values for the archetypes (Table 2). In addition, the distributions of fault parameters of wrinkle ridge and lobate scarp archetypes either overlap or form a continuum, as seen in the first and third quartile values of wrinkle ridge archetypes beginning or ending where those of lobate scarp archetypes end or begin (see position of boxes in Figure 7).

The most notable difference between archetype types is the *number* of faults, and the least amount of overlap occurs in the *depth* of faulting. A typical lobate scarp archetype was modeled using one listric thrust fault that penetrated to depths of ~27 km (e.g., Figure 6a) whereas a typical wrinkle ridge archetype was modeled with 2 faults (Table 2) and penetrates only to depths of ~13 km (e.g., Figure 6c). The differences between wrinkle ridge and lobate scarp archetypes are likely to arise differences in host lithology. Most of the wrinkle ridge archetypes in this study are situated in the smooth plains units, whereas most of the lobate scarp archetypes are located in the intercrater plains units (Figure 2). Regardless, with an average depth of faulting of 13 km, wrinkle ridge archetypes penetrate deeper than estimates of up to 2 km for the depth of the volcanic emplacements that make up the smooth plains units (Head et al., 2011; Ostrach et al., 2015; Du et al., 2020). This geometry suggests that the mechanisms that produce lobate scarp and wrinkle ridge archetypes are the same. However, geographically, the lithosphere underlying the smooth plains units may have hosted very deeply penetrating thrust faults, the surface expression of which would have been muted by the subsequent emplacement of relatively well-layered smooth plains. These newer mechanical layers were not present in the intercrater plains, and such faulting underneath the smooth plains lava emplacements may have been reactivated upward, creating the shortening landforms observed in these units without slip occurring at deeper depths. When a geologically younger, thin unit of rock is placed on top of a faulted rock volume and is then mechanically faulted through, more complex deformation in the upper layer is caused by the basement-reactivated fault.

Both endmember types vary widely in subsurface geometry, with some wrinkle ridge archetypes being modeled with single faults and some lobate scarp members hosting multi-fault thrust systems. These results illustrate further that the “typical” archetype lobate scarp and wrinkle ridge structures show some differences, but that the spectrum of thrust architecture underlying both of these landform types shows substantial overlap. These findings echo those of Loveless et al. (2024a), further corroborating that shortening landforms on Mercury’s surface exist on a spectrum between the traditional nomenclature of lobate scarps and wrinkle ridges.

5.2) Tectonic Architecture of Thrust Systems on Mercury

All shortening landforms in this study are underlain by listric faults (e.g., Figure 6). The typical lobate scarp archetype structure contains only a single, listric fault. Shortening landforms that are modeled with more than one fault may either be constructed with multiple listric faults, or the secondary (and possibly tertiary) faults may have a more homoclinal geometry (e.g., the secondary faults in Figure 6c and Figure 8). The listric geometry of the fault is what dictates the shape of the overlying topography in a fault-bend fold. When comparing lobate scarps on Mercury with tectonic deformational features on Earth, Byrne et al. (2018) had described lobate scarps "as upthrust volumes of rock that are likely the folded portions of hanging walls atop of thrust faults." This analogy describes lobate scarps that have formed from surface breaking thrusts on Mercury as fault-bend folds.

Previous studies using the COULOMB dislocation modeling found listric faults to be a viable architecture underlying contractional tectonics on terrestrial planets (e.g., Watters and Schultz, 2002; Peterson et al., 2020). However, these studies also show that listric faults and homoclinal faults generate similar topography, suggesting non-unique solutions. Other studies using the same modeling technique have argued that listric faults fail to accurately generate observed topography (e.g., Egea-González et al., 2012; Herrero-Gil et al., 2019). This modeling technique does not consider folding. If the hanging wall is faulted over the footwall at the surface, it will likely fold over the fault. By using a fault-bend-fold geometry, our models replicate this folding. In a fault-bend-fold model, the listric shape of the underlying fault greatly affects the way the surface folds after the input shortening is applied. The change in dip along a listric geometry affects the displacement along the fault as governed by the same trigonometric relationships described by a ramp-up structure in Suppe (1983).

A typical archetype wrinkle ridge structure requires two or more faults to accurately replicate topographic observations (Figure 7c). Pop-up structures are more common than imbricate thrusts for multi-fault thrust systems used to model wrinkle ridge archetypes. For wrinkle ridge archetypes, we see that the folding of the hanging wall produced by the pop-up structure creates a plateau flanked on either side by monoclines that are folded over their fault plains. This agrees with previously proposed structural interpretations of wrinkle ridges (Byrne et al., 2018). Slope-asymmetry analysis of wrinkle ridges on Mars supports similar geometries (Okubo and Schultz, 2004). These Martian wrinkle ridges are the accumulation of a primary thrust and secondary back and fore thrusts that branch off the primary thrust. We find some similar subsurface geometries for shortening landforms with opposing thrust-fault vergence. However, the wrinkle ridge archetypes on Mercury described here have greater relief than the Martian landforms analyzed in Okubo and

Schultz (2004). We also find simpler fault architectures to be able to replicate many of our wrinkle ridge archetypes than some of the geometries suggested by Okubo and Schultz (2004). Additionally, contractional tectonics on Earth that result in a hanging-wall folding over the thrust and footwall (e.g., Petterson et al., 1997; Last et al., 2012) are frequently used as analogous structures for contractional tectonics on other terrestrial planets (e.g., Plescia and Golombek, 1986; Watters, 1988; Crane and Klimczak, 2019b; Crane, 2020b). The results presented here then suggest that fault-bend fold architectures should be further utilized when structurally assessing contractional tectonics in Mercury's smooth plains.

Imbricate thrust structures are the least common fault geometry we model in our sample of shortening landforms. Only two lobate scarp archetypes and five wrinkle ridge archetypes were modeled as imbricate thrusts. The small sample size of multi-fault lobate scarp archetypes is likely a result of the sample selection process, as the LDA in Loveless et al. (2024a) classified the most endmember lobate scarps by their larger sizes. The size of these structures may be indication that the faults matured to the point that previous imbricate thrusts linked into a large singular fault plane, indicative of how Cowie and Scholz (1992) suggest faults grow within the Earth's lithosphere. Alternatively, more shortening landforms occupy the geologically younger smooth plains than the geologically older intercrater plains units (Byrne et al., 2014). The concentration of shortening landforms in the smooth plains attests to the greater number of shortening landforms we modeled in the smooth plains to host more than one fault in the underlying structure. However, many shortening landforms on Mercury display multiple sub-parallel to parallel surface breaks similar in photogeology to the imbricate thrusts modeled here (e.g., Crane and Klimczak, 2019b). Expanding the sample size of this work may then increase the shortening landforms in the intercrater plains units.

5.3) Implications for Mercury Tectonics

Many studies use the vertical relief of a structure as equal to the throw of the underlying fault to infer the displacement along the fault plane (e.g., Watters et al., 2001; Byrne et al., 2014; Klimczak et al., 2018; Watters, 2021). Friction theory predicts optimal dip angles for thrust faults in a basaltic rock volume to be ~31° and thus displacements are typically inferred for angles of 30°±5°. Results of our analysis show that the average and maximum dip angles of thrust faults on Mercury are ~22° to ~40°, respectively (Table 2). This is a larger range of dip angles of thrust faults than used previously, including thrust faults with much shallower and steeper dips. Our results thus warrant considerations of a wider range of dip angles for any analysis inferring thrust fault displacements from measurements of structural relief. Using the traditional method of deriving shortening strain for planetary thrust faults (e.g., Byrne et al., 2014; Watters, 2021), an average dip value of ~22° would increase previous estimates of Mercury's global strain whereas an angle of 40° would reduce strain estimates (e.g., Byrne et al., 2014; Watters 2021). The larger range of dip angles found in this study suggests that previous assumptions of the range of dip angles for Mercury's population of thrust faults yielded a too narrow range of strain estimates.

Enterprise Rupes is a shortening landform that Galluzzi et al. (2015) assessed with crosscut craters. They found a large range of dip angles for the faults underlying Enterprise Rupes, ranging from 15°±5° to 57°±16°, which agrees well with our range of modeled dips. Our results indicate that Enterprise Rupes has an average dip angle of ~10° and a maximum dip of 21° close to the surface, agreeing well with the lower estimates of two of the three crosscut craters near our transect. However, the crater evaluated by Galluzzi et al. (2015) that is closest to our transect has the steepest dip angles. This mismatch may be due to the degradational state of this crater or to the natural complexity of the fault system in this area. Galluzzi et al. (2015) consider a single fault when assessing the deformation of this crater, while multiple faults are required to match the map pattern and topography of Enterprise Rupes. If this crater was deformed by two opposing faults, this may explain the mismatch between the two analyses.

A second shortening landform in our study also crosscuts a crater assessed by Galluzzi et al. (2015) (their Crater 05-C). We find a near-surface dip angle and average dip angle of 29° and 30°, respectively, which is relatively close to the dip angle range of 20° ± 3° reported in Galluzzi et al. (2015). The discrepancies of our results may be due to the fact that a crosscut crater only captures the local, near-surface dip of the fault. Our modeling efforts capture the broader structure and take into account the topography beyond the extent of the crater.

The mean of the average dips for our modeled lobate scarp archetypes averages at ~27° for all models. This value agrees with previous modeling results of individual or small sets of shortening landforms (e.g., Schultz and Watters, 2001; Egea-González et al., 2012; Egea-González et al., 2017). The mean of the maximum dips for lobate scarp archetypes is ~43°, with a few individual structures even showing maximum dips of ~60° (Figure 7c), which is rather atypical for thrust faults. However, our wrinkle ridge archetypes have an average dip of ~19°. This value is considerably less than the range of dip angles found in COULOMB dislocation modeling efforts by Peterson et al. (2020). Multiple models constructed in Peterson et al. (2020) were shown to produce similar topographies for the same shortening landform and listric fault geometries were created by using a step curvature function from one fault tip to the other. In our study we find that folding at the surface plays a substantial role in dictating the depth and dip angle of our faults. The COULOMB modeling software cannot take into account distortion from folding and instead assumes fully elastic deformation around the fault from a single faulting event, scaled up to the shape of the landforms after many slip events, which becomes unrealistic for the large displacements associated with these shortening landforms. This limitation in COULOMB is likely the reason for the discrepancy in dip angles for wrinkle ridge archetypes in the two approaches.

Our models indicate a wide range of depths of faulting for all shortening landforms. The average depth of faulting for all modeled shortening landforms is ~22 km and shortening landforms inside the intercrater plains fault to an average depth of ~27 km. Intercrater plains likely are composed of a brittle volume of basaltic crust that may act as a single mechanical unit. The greatest penetration depths we find extend to ~48 km (Figure 7b), suggested that the faulted volume of Mercury's lithosphere reaches depths perhaps as much as 50 km. Previous studies that have investigated the depth extent of faulting for shortening landforms on Mercury provide similar values, such as 25–40 km for faults in the intercrater plains (e.g., Watters and Schultz 2002; Ritzer et al., 2010; Egea-González et al., 2012).

Alternatively, the basaltic lava emplacements of the smooth plains units are only estimated to be only a few hundred meters to up to ~2 km thick and they sit on top of basement rock (Head et al., 2011; Ostrach et al., 2015; Du et al., 2020). The modeled average depth of faulting of 13 km for the wrinkle ridge archetypes in this study greatly exceeds these thickness estimates. This model depth indicates that many of the modeled wrinkle ridge archetypes are not by any measure constrained to within the smooth plains units. Previous work has also suggested that smooth plains structures can fault to comparable depths to intercrater plains structures (e.g., Peterson et al., 2020). In these geographic regions, Mercury's lithosphere is composed of volcanic deposits overlaying mechanically weak layers of rock due to impacts. Therefore, there are likely multiple mechanical interfaces of different deformed basaltic layers, and so the terms thin and thick-skinned tectonics as described for Earth's tectonics by Pfiffner (2017) are likely an inaccurate way to structurally describe Mercurian tectonics. However, we find that these faulting depths for wrinkle ridge archetypes agree with the term "basement involved thin-skinned tectonics" attributed to Mercury's tectonics by Crane and Klimczak (2019b). In this case, the deformation in the smooth plains units are influenced by the faulting in the underlying basement rock such that deformation in the basement produces a series of structural geometries and patterns in the smooth plains that are characteristic of thin-skinned deformation. Many of our wrinkle ridge archetype models are consistent with basement involved thin-skinned tectonics, where, for example, pop-up structures that reside in the smooth plains units typically contain a primary fault that penetrates 10 km below the surface but the secondary fault only penetrating no deeper than ~ 3 km (Figure 6c). In a 2–3 km thick smooth plains units, then, these secondary faults may be the result of more complex deformation occurring solely within these unit but that connect to, and were initiated by faulting at depth, in the underlying basement rock. The mechanically distinct plains units may then partition strain off of the primary, deeply rooted thrust, resulting in additional faults and folds that are only confined to the smooth plains units. This is similar to the process described by Crane and Klimczak (2019b) for contractional tectonics in Mercury's smooth plains units where thrusts rooted in the underlying lithosphere causes deformation in the overlying, mechanically-weak layer.

Wrinkle ridges in the smooth plains units on Mercury have been compared with shortening structures in the lunar maria, with those landforms on the Moon being ascribed to loading-induced subsidence with contributions from global contraction (Schleicher et al., 2019). However, loading-induced subsidence is inconsistent with basement-involved thin-skinned thrust tectonics and a formation of such structures on Mercury by global contraction alone is more plausible. In fact, thrust faults underlying shortening landforms described as wrinkle ridges found in several mare units in lunar mascon basins are found to be deep-seated (Byrne et al., 2016; Collins et al., 2023). Their origin is ascribed to mascon tectonics (Byrne et al., 2015), and their continued growth and surface expression in the surficial mare units did not require loading stresses from the mare units whereas contributions of stresses from the lunar global contraction are plausible (Byrne et al., 2015).

We do not detect a systematic pattern of the distribution of shortening strains across Mercury, albeit wrinkle ridge archetypes tend to produce somewhat less strain than lobate scarp archetypes. However, the variance of shortening strain from wrinkle ridge archetypes and lobate scarp archetypes overlaps substantially (Figure 7f). These findings agree with previous studies that observed geologic trends in morphology and timing (e.g., Banks et al., 2015; Crane and Klimczak, 2019b; Peterson et al., 2019). If global contraction were the source of stresses driving faulting, there would be no systematic pattern of strain distribution expected, even if it overlapped with other processes. Other processes that have been invoked for Mercury to produce global fracture patterns like despinning (e.g., Melosh, 1977; Matsuyama and Nimmo, 2009) or reorientation (Matsuyama and Nimmo, 2009) would only influence the orientation of fracture patterns (Klimczak et al. 2023) when working in conjunction with global contraction. However, the shortening strain of the landforms likely would not have a global systematic pattern if global contraction is the primary source of stresses to cause faulting.

6) Conclusions

We investigated the thrust fault geometries beneath 55 shortening landforms on Mercury. We specifically selected wrinkle ridge and lobate scarp archetypes to highlight the differences in thrust system geometries that are present within Mercury's lithosphere. We find that while Mercury hosts diverse thrust systems, including single, listric faults, imbricate thrusts, and pop-up structures, the thrust fault geometries of wrinkle ridge and lobate scarp archetypes overlap or form a continuum (Figure 7). This overlap and continuation in range of fault geometric parameters confirm our previous results (Loveless et al., 2024a), where shortening landforms on Mercury form a spectrum of landform shapes rather than discrete categories. The results of the work presented here further illustrates the impracticality of traditional "lobate scarp" and "wrinkle ridge" nomenclature to describe landforms that are much more similar than they are different.

We find a large range of fault geometric parameters for the thrust systems that underly Mercury's shortening landforms. The average fault dip of all the structures ranges from ~22° and to ~40°. We also find that the deepest fault penetrates Mercury's lithosphere to 48 km, whereas the average depth of faulting for all studied structures is 22 km. These parameters may serve to better constrain future studies estimating fault strain or analyzing lithospheric structure on Mercury.

Our modeling results inform an understanding of Mercury's tectonic character. The shortening landforms that reside in Mercury's smooth plains units are likely caused by the basement involved thin-skin tectonics mechanism suggested by Crane and Klimczak (2019b), with thrusts penetrating well below the lavas that makeup the smooth plains units. As the faults penetrate deep into the underlying basement rock and show no noticeable difference in strain compared with faults in intercrater plains, the formation of these thrusts by loading-induced subsidence can be ruled out and instead are likely to have been primarily driven by global contraction.

7) Acknowledgements

The research presented here was funded by NASA's SSW program under grant 20-SSW20-0153. We make use of 14 MESSENGER products available on the PDS Geoscience Node in the MDIS archive specifically in node PDS3 and in the MLA archive in node PDS4. We thank PE Limited (Petex) for their donation of academic licenses of the MOVE modeling software to the University of Georgia.

8) Data Availability

The supplementary material for this research is available on Mendeley Data at Loveless et al. (2024c): https://data.mendeley.com/datasets/k4yrmr5j6k/1.

9) References

Bally, A. W., Gordy, P.L., and Steward, GA., 1966. Structure, seismic data and orogenic evolution of the southern Canadian Rocky Mountains. Bull. Can. Petrol. Geol. 14, 337–381.

Banks, M.E., Xiao, Z., Watters, T.R., Strom, R.G., Braden, S.E., Chapman, C.R., Solomon, S.C., Klimczak, C., Byrne, P.K., 2015. Duration of activity on lobate-scarp thrust faults on Mercury. Journal of Geophysical Research: Planets 120, 1751–1762. https://doi.org/10.1002/2015je004828

Bertone, S., Mazarico, E., Barker, M.K., Siegler, M.A., Martinez-Camacho, J.M., Hamill, C.D., Glantzberg, A.K., Chabot, N.L., 2023. Highly Resolved Topography and Illumination at Mercury's South Pole from MESSENGER MDIS NAC. Planet. Sci. J. 4, 21. https://doi.org/10.3847/psj/acaddb

Boyer, S. E., and Elliot, D. 1982. Thrust Systems. AAPG Bulletin, 66. https://doi.org/10.1306/03b5a77d-16d1-11d7-8645000102c1865d

Brandes, C., Tanner, D.C., 2014. Fault-related folding: A review of kinematic models and their application. Earth-Science Reviews 138, 352–370. https://doi.org/10.1016/j.earscirev.2014.06.008

Butler, R.W. H., 1987. Thrust sequences. Journal of the Geological Society 144, 619–634. https://doi.org/10.1144/gsjgs.144.4.0619

Byrne, P. K., Klimczak, C., and LaFond, J. K., 2016. The East Kaibab monocline: A Terran lobate scarp? Lunar Planet. Sci. XLVII. Abstract 1022.

Byrne, P.K., Klimczak, C., Şengör, A.M.C., Solomon, S.C., Watters, T.R., II, S.A.H., 2014. Mercury's global contraction much greater than earlier estimates. Nat Geosci 7, 301–307. https://doi.org/10.1038/ngeo2097

Byrne, P.K., Klimczak, C., McGovern, P.J., Mazarico, E., James, P.B., Neumann, G.A., Zuber, M.T., Solomon, S.C., 2015. Deep-seated thrust faults bound the Mare Crisium lunar mascon. Earth and Planetary Science Letters 427, 183–190. https://doi.org/10.1016/j.epsl.2015.06.022

Byrne, P.K., Klimczak, C., Şengör, A., 2018. The tectonic character of Mercury. IN: Solomon, S.C. (Ed.), Mercury. The View after MESSENGER. Pp. 249–286.

Chapple, W.M., 1978. Mechanics of thin-skinned fold-and-thrust belts. GSA Bulletin 89, 1189–1198. https://doi.org/10.1130/0016-7606(1978)89<1189:motfb>2.0.co;2

Collins, M.S., Byrne, P.K., Klimczak, C., Mazarico, E., 2023. Thrust Faults Bound an Elevated Mantle Plug Beneath Several Lunar Basins. Journal of Geophysical Research: Planets 128. https://doi.org/10.1029/2022je007682

Connors, C.D., Hughes, A.N., Ball, S.M., 2021. Forward kinematic modeling of fault-bend folding. Journal of Structural Geology 143, 104252. https://doi.org/10.1016/j.jsg.2020.104252

Cowie, P.A., Scholz, C.H., 1992. Displacement-length scaling relationship for faults: data synthesis and discussion. Journal of Structural Geology 14, 1149–1156. https://doi.org/10.1016/0191-8141(92)90066-6

Crane, K.T., Klimczak, C., 2019a. A 3-D structural model of the Saddle Mountains, Yakima Fold Province, Washington, USA: Implications for Late Tertiary tectonic evolution of the Columbia River Flood Basalt Province. Tectonophysics 766, 1–13. https://doi.org/10.1016/j.tecto.2019.05.015

Crane, K.T., Klimczak, C., 2019b. Tectonic patterns of shortening landforms in Mercury's northern smooth plains. Icarus 317, 66–80. https://doi.org/10.1016/j.icarus.2018.05.034

Crane, K., 2020a. Structural interpretation of thrust fault-related landforms on Mercury using Earth analogue fault models. Geomorphology 369, 107366. https://doi.org/10.1016/j.geomorph.2020.107366

Crane, K., 2020b. Approach and application of industry software to structural investigations in the subsurface of Mercury's thrust fault-related landforms. Journal of Structural Geology 141, 104218. https://doi.org/10.1016/j.jsg.2020.104218

Dahlstrom, C.D.A., 1969. Balanced cross sections. Canadian Journal of Earth Sciences 6, 743–757. https://doi.org/10.1139/e69-069

Denevi, B.W., Chabot, N.L., Murchie, S.L., Becker, K.J., Blewett, D.T., Domingue, D.L., Ernst, C.M., Hash, C.D., Hawkins, S.E., Keller, M.R., Laslo, N.R., Nair, H., Robinson, M.S., Seelos, F.P., Stephens, G.K., Turner, F.S., Solomon, S.C., 2017. Calibration, Projection, and Final Image Products of MESSENGER's Mercury Dual Imaging System. Space Science Reviews 214, 2.

Denevi, B.W., Ernst, C.M., Meyer, H.M., Robinson, M.S., Murchie, S.L., Whitten, J.L., Head, J.W., Watters, T.R., Solomon, S.C., Ostrach, L.R., Chapman, C.R., Byrne, P.K., Klimczak, C., Peplowski, P.N., 2013. The distribution and origin of smooth plains on Mercury. Journal of Geophysical Research: Planets 118, 891–907. https://doi.org/10.1002/jgre.20075

Du, J., Wieczorek, M.A., Fa, W., 2020. Thickness of Lava Flows Within the Northern Smooth Plains on Mercury as Estimated by Partially Buried Craters. Geophysical Research Letters 47. https://doi.org/10.1029/2020gl090578

Dzurisin, D., 1978. The tectonic and volcanic history of Mercury as inferred from studies of scarps, ridges, troughs, and other lineaments. J Geophys Res Solid Earth 83, 4883–4906. https://doi.org/10.1029/jb083ib10p04883

Egan, S.S., Buddin, T.S., Kane, S., Williams, G.D., 1997. Three-dimensional modelling and visualisation in Structural Geology: New Techniques for the restoration and balancing of volumes. Electronic Geology 1, 67–82.

Egea-González, I., Ruiz, J., Fernández, C., Williams, J.-P., Márquez, Á., Lara, L.M., 2012. Depth of faulting and ancient heat flows in the Kuiper region of Mercury from lobate scarp topography. Planetary and Space Science 60, 193–198. https://doi.org/10.1016/j.pss.2011.08.003

Egea-Gonzalez, I., Jiménez-Díaz, A., Parro, L.M., López, V., Williams, J.-P., Ruiz, J., 2017. Thrust fault modeling and Late-Noachian lithospheric structure of the circum-Hellas region, Mars. Icarus 288, 53–68. https://doi.org/10.1016/j.icarus.2017.01.028

Ferrari, S., Massironi, M., Marchi, S., Byrne, P.K., Klimczak, C., Martellato, E., Cremonese, G., 2015. Age relationships of the Rembrandt basin and Enterprise Rupes, Mercury. Geological Society, London, Special Publications 401, 159–172. https://doi.org/10.1144/sp401.20

Galluzzi, V., Achille, G.D., Ferranti, L., Popa, C., Palumbo, P., 2015. Faulted craters as indicators for thrust motions on Mercury. Geological Society, London, Special Publications 401, 313–325. https://doi.org/10.1144/sp401.17

Golombek, M.P., Anderson, F.S., Zuber, M.T., 2001. Martian wrinkle ridge topography: Evidence for subsurface faults from MOLA. Journal of Geophysical Research: Planets 106, 23811–23821. https://doi.org/10.1029/2000je001308

Head, J.W., Chapman, C.R., Strom, R.G., Fassett, C.I., Denevi, B.W., Blewett, D.T., Ernst, C.M., Watters, T.R., Solomon, S.C., Murchie, S.L., Prockter, L.M., Chabot, N.L., Gillis-Davis, J.J., Whitten, J.L., Goudge, T.A., Baker, D.M.H., Hurwitz, D.M., Ostrach, L.R., Xiao, Z., Merline, W.J., Kerber, L., Dickson, J.L., Oberst, J., Byrne, P.K., Klimczak, C., Nittler, L.R., 2011. Flood volcanism in the northern high latitudes of Mercury revealed by MESSENGER. Science (New York, N.Y.) 333, 1853–6. https://doi.org/10.1126/science.1211997

Herrero-Gil, A., Ruiz, J., Romeo, I., 2019. 3D modeling of planetary lobate scarps: The case of Ogygis Rupes, Mars. Earth and Planetary Science Letters 532, 116004. https://doi.org/10.1016/j.epsl.2019.116004

Herrero-Gil, A., Ruiz, J., Romeo, I., 2020. Lithospheric Contraction on Mars: A 3D Model of the Amenthes Thrust Fault System. Journal of Geophysical Research: Planets 125. https://doi.org/10.1029/2019je006201

Hopgood, A.M. (1987). Imbricate structure. In: Structural Geology and Tectonics. Encyclopedia of Earth Science. Springer, Berlin, Heidelberg. https://doi.org/10.1007/3-540-31080-0_50

Hughes, A.N., Benesh, N.P., Shaw, J.H., 2014. Factors that control the development of fault-bend versus fault-propagation folds: Insights from mechanical models based on the discrete element method (DEM). Journal of Structural Geology 68, 121–141. https://doi.org/10.1016/j.jsg.2014.09.009

Jackson, J., McKenzie, D., 1983. The geometrical evolution of normal fault systems. Journal of Structural Geology 5, 471–482. https://doi.org/10.1016/0191-8141(83)90053-6

Klimczak, C., Crane, K.T., Byrne, P.K., 2023. Revealing multiple global tectonic patterns on Mercury. Lunar Planet Sci LIV. Abstract 1122.

Last, G.V., Winsor, K., Unwin, S.D., 2012. A Summary of Information on the Behavior of the Yakima Fold Belt as a Structural Entity -- Topical Report. https://doi.org/10.2172/1053763

Loveless, S.R., Klimczak, C., McCullough, L.R., Crane, K.T., Holland, S.M., Byrne, P.K., 2024a. A statistical evaluation of the morphological variability of shortening landforms on Mercury. Icarus 416, 116106. https://doi.org/10.1016/j.icarus.2024.116106

Loveless, S., Klimczak, C., McCullough, L., Crane, K., Holland, S., Byrne, P., 2024b. Code and Data for ‘A statistical evaluation of the morphological variability of shortening landforms on Mercury.’. Revised, Mendeley Data V2. https://doi.org/10.17632/ 8968vkgpds.2.

Loveless, S., Klimczak, C., Crane, K., Byrne, P., 2024c. Models, topographic profiles, and data for ‘Geometric forward modeling of thrust systems underlying shortening landforms on Mercury.’, Mendeley Data, V1, https://doi.org/10.17632/k4yrmr5j6k.1.

Matsuyama, I., Nimmo, F., 2009. Gravity and tectonic patterns of Mercury: Effect of tidal deformation, spin-orbit resonance, nonzero eccentricity, despinning, and reorientation. Journal of Geophysical Research: Planets 114. https://doi.org/10.1029/2008je003252

Matthews, V., Work, D.F., 1978. Laramide Folding Associated with Basement Block Faulting in the Western United States. Geological Society of America Memoirs 101–124. https://doi.org/10.1130/mem151-p101

McClay, K.R., 1978. Thrust and nappe tectonics. Tectonophysics 50, 79. https://doi.org/10.1016/0040-1951(78)90200-7

McClay, K. R., and Price, N. J. (1981). (Eds.), *Thrust and Nappe Tectonics*, Spec. Publ. 9, 539 pp., Geological Society of London, Oxford.

Melosh, H.J., 1977. Global tectonics of a despun planet. Icarus 31, 221–243. https://doi.org/10.1016/0019-1035(77)90035-5

Melosh, H. J. and McKinnon, W. B., 1988. The tectonics of Mercury. In: Vilas, F., Chapman, C. R., Matthews, M. S. (Eds.), Mercury. pp. 374–400.

Morley, C.K., 1988. Out-of-Sequence Thrusts. Tectonics 7, 539–561. https://doi.org/10.1029/tc007i003p00539

Mueller, K., Vidal, A., Robbins, S., Golombek, M., West, C., 2014. Fault and fold growth of the Amenthes uplift: Implications for Late Noachian crustal rheology and heat flow on Mars. Earth and Planetary Science Letters 408, 100–109. https://doi.org/10.1016/j.epsl.2014.09.047

Nahm, A.L., Watters, T.R., Johnson, C.L., Banks, M.E., Bogert, C.H. van der, Weber, R.C., Andrews-Hanna, J.C., 2023. Tectonics of the Moon. Reviews in Mineralogy and Geochemistry 89, 691–727. https://doi.org/10.2138/rmg.2023.89.16

Nimmo, F., Watters, T.R., 2004. Depth of faulting on Mercury: Implications for heat flux and crustal and effective elastic thickness. Geophysical Research Letters 31. https://doi.org/10.1029/2003gl018847

Okubo, C.H., Schultz, R.A., 2004. Mechanical stratigraphy in the western equatorial region of Mars based on thrust fault–related fold topography and implications for near-surface volatile reservoirs. GSA Bulletin 116, 594–605. https://doi.org/10.1130/b25361.1

Ostrach, L.R., Robinson, M.S., Whitten, J.L., Fassett, C.I., Strom, R.G., Head, J.W., Solomon, S.C., 2015. Extent, age, and resurfacing history of the northern smooth plains on Mercury from MESSENGER observations. Icarus 250, 602–622. https://doi.org/10.1016/j.icarus.2014.11.010

Pierdominici, S., Mariucci, M.T., Montone, P., 2011. A study to constrain the geometry of an active fault in southern Italy through borehole breakouts and downhole logs. Journal of Geodynamics 52, 279–289. https://doi.org/10.1016/j.jog.2011.02.006

Peterson, G.A., Johnson, C.L., Byrne, P.K., Phillips, R.J., 2019. Distribution of Areal Strain on Mercury: Insights Into the Interaction of Volcanism and Global Contraction. Geophysical Research Letters 46, 608–615. https://doi.org/10.1029/2018gl080749

Peterson, G.A., Johnson, C.L., Byrne, P.K., Phillips, R.J., 2020. Fault Structure and Origin of Compressional Tectonic Features Within the Smooth Plains on Mercury. Journal of Geophysical Research: Planets 125. https://doi.org/10.1029/2019je006183

Petterson, M.G., Neal, C.R., Mahoney, J.J., Kroenke, L.W., Saunders, A.D., Babbs, T.L., Duncan, R.A., Tolia, D., McGrail, B., 1997. Structure and deformation of north and central Malaita, Solomon Islands: tectonic implications for the Ontong Java Plateau-Solomon arc collision, and for the fate of oceanic plateaus. Tectonophysics 283, 1–33. https://doi.org/10.1016/s0040-1951(97)00206-0

Pfiffner, O.A., 2017. Thick-Skinned and Thin-Skinned Tectonics: A Global Perspective. Geosciences 7, 71. https://doi.org/10.3390/geosciences7030071

Plescia, J.B., Golombek, M.P., 1986. Origin of planetary wrinkle ridges based on the study of terrestrial analogs. GSA Bull. 97, 1289–1299. https://doi.org/10.1130/0016-7606(1986)97<1289:oopwrb>2.0.co;2

Ritzer, J.A., Hauck, S.A., Barnouin, O.S., Solomon, S. C., Watters, T.R., 2010. Mechanical structure of Mercury’s lithosphere from MESSENGER observations of lobate scarps. Lunar Planet Sci XLI. Abstract 2122.

Rothery, D.A., Massironi, M., 2010. Beagle Rupes – Evidence for a basal decollement of regional extent in Mercury’s lithosphere. Icarus 209, 256–261. https://doi.org/10.1016/j.icarus.2009.12.009

Schleicher, L.S., Watters, T.R., Martin, A.J., Banks, M.E., 2019. Wrinkle ridges on Mercury and the Moon within and outside of mascons. Icarus 331, 226–237. https://doi.org/10.1016/j.icarus.2019.04.013

Schultz, R.A., 2000. Localization of bedding plane slip and backthrust faults above blind thrust faults: Keys to wrinkle ridge structure. Journal of Geophysical Research: Planets 105, 12035–12052. https://doi.org/10.1029/1999je001212

Schultz, R.A., Watters, T.R., 2001. Forward mechanical modeling of the Amenthes Rupes Thrust Fault on Mars. Geophys. Res. Lett. 28, 4659–4662. https://doi.org/10.1029/2001gl013468

Shaw, J.H., Connors, C., Suppe, J. (Eds.), 2005. Seismic Interpretation of Contractional Fault-Related Folds, Studies in Geology. American Association of Petroleum Geologists. https://doi.org/10.1306/st531003

Smythe, DK., Dobinson, A., McQuillan, R., Brewer, J.A., Matthews, D.H., Blundell, D.J., and Kelk, B., 1982. Deep Structure of the Scottish Calendonides revealed by the MOIST reflection profile. Nature, Lond. 199, 338–340.

Solomon, S.C., 1977. The relationship between crustal tectonics and internal evolution in the moon and Mercury. Physics of the Earth and Planetary Interiors 15, 135–145. https://doi.org/10.1016/0031-9201(77)90026-7

Solomon, S.C., 1978. On volcanism and thermal tectonics on one-plate planets. Geophys. Res. Lett. 5, 461–464. https://doi.org/10.1029/gl005i006p00461

Strom, R.G., Trask, N.J., Guest, J.E., 1975. Tectonism and volcanism on Mercury. J. Geophys. Res. 80, 2478–2507. https://doi.org/10.1029/jb080i017p02478

Strom, R.G., 1979. Mercury: A post-Mariner 10 assessment. Space Science Reviews 24, 3–70. https://doi.org/10.1007/bf00221842

Suppe, J., 1983. Geometry and kinematics of fault-bend folding. American Journal of Science 283, 684–721. https://doi.org/10.2475/ajs.283.7.684

Suppe, J., Namson, J., 1979. Fault-bend origin of front folds of the western Taiwan fold-and-thrust belt. Petroleum Geology of Taiwan 16, 1–18.

Toda, S., Stein, R.S., Richards-Dinger, K., Bozkurt, S.B., 2005. Forecasting the evolution of seismicity in southern California: Animations built on earthquake stress transfer. Journal of Geophysical Research: Solid Earth 110. https://doi.org/10.1029/2004jb003415

Tosi, N., Grott, M., Plesa, A. -C., Breuer, D., 2013. Thermochemical evolution of Mercury's interior. Journal of Geophysical Research: Planets 118, 2474–2487. https://doi.org/10.1002/jgre.20168

Watters, T.R., 1988. Wrinkle ridge assemblages on the terrestrial planets. Journal of Geophysical Research: Solid Earth 93, 10236–10254. https://doi.org/10.1029/jb093ib09p10236

Watters, T.R., 2003. Lithospheric flexure and the origin of the dichotomy boundary on Mars. Geology 31, 271–274. https://doi.org/10.1130/0091-7613(2003)031<0271:lfatoo>2.0.co;2

Watters, T.R., 1993. Compressional tectonism on Mars. J Geophys Res 98, 17049. https://doi.org/10.1029/93je01138

Watters, T.R., 2021. A case for limited global contraction of Mercury. Communications Earth & Environment 2, 9. https://doi.org/10.1038/s43247-020-00076-5

Watters, T.R., Cook, A.C., Robinson, M.S., 2001. Large-scale lobate scarps in the southern hemisphere of Mercury. Planetary and Space Science 49, 1523–1530. https://doi.org/10.1016/s0032-0633(01)00090-3

Watters, T.R., Montési, L.G.J., Oberst, J., Preusker, F., 2016. Fault-bound valley associated with the Rembrandt basin on Mercury. Geophysical Research Letters 43, 11,536-11,544. https://doi.org/10.1002/2016gl070205

Watters, T.R., Nimmo, F., 2010. The tectonics of Mercury. In: Watters, T.R., Schultz, R.A. (Eds.), Planetary Tectonics, pp. 15–80. https://doi.org/10.1017/cbo9780511691645.002.

Watters, T.R., Robinson, M.S., 1999. Lobate scarps and the Martian crustal dichotomy. Journal of Geophysical Research: Planets 104, 18981–18990. https://doi.org/10.1029/1998je001007

Watters, T.R., Solomon, S.C., Robinson, M.S., Head, J.W., André, S.L., Hauck, S.A., Murchie, S.L., 2009. The tectonics of Mercury: The view after MESSENGER's first flyby. Earth and Planetary Science Letters 285, 283–296. https://doi.org/10.1016/j.epsl.2009.01.025

Watters, T.R., Robinson, M.S., Bina, C.R., Spudis, P.D., 2004. Thrust faults and the global contraction of Mercury. Geophys Res Lett 31. https://doi.org/10.1029/2003gl019171

Watters, T.R., Schultz, R.A., 2002. The fault geometry of planetary lobate scarps: Listric versus planar. Lunar Planet. Sci. XXXIII. Abstract 1668.

Wickham, J., 1995. Fault displacement-gradient folds and the structure at Lost Hills, California (U.S.A.). Journal of Structural Geology 17, 1293–1302. https://doi.org/10.1016/0191-8141(95)00029-d

Williams, N.R., Watters, T.R., Pritchard, M.E., Banks, M.E., Bell, J.F., 2013. Fault dislocation modeled structure of lobate scarps from Lunar Reconnaissance Orbiter Camera digital terrain models. Journal of Geophysical Research: Planets 118, 224–233. https://doi.org/10.1002/jgre.20051